

X-Ray Nanoanalysis Revealing the Role of Electronically Active Passivation Layers in Perovskite X-Ray film Detectors

Matteo Verdi, Andrea Ciavatti,* Jaime Segura-Ruiz, Laura Basiricò, Roberto Sorrentino, Isabel Pinto Goncalves, Annamaria Petrozza, Federico Boscherini,* and Beatrice Fraboni

X-ray direct detectors based on hybrid lead-halide perovskite have seen a dramatic increase of interest in the last years. A rush for the achievement of high performing devices drives the scientific community. In this context, several photoconductor sensors employ functional layers to increase the gain effect, but the full comprehension of the mechanism is still lacking. Here X-ray nanoanalysis is used, performed by simultaneous acquisition of X-ray Fluorescence and X-ray Beam Induced Current maps, to investigate at the nanoscale level the role of [6,6]-phenyl-C61-butyric acid methyl ester fullerene (PCBM) molecules when interacting with MAPbI₃ polycrystalline thin films acting as photo-conductors in X-ray detectors. At the device-scale level it shows that the addition of PCBM enhances the X-ray sensitivity by four times. At the nanoscale level how the perovskite grain boundaries act as high photocurrent generation centers is demonstrated. The addition of the PCBM increases the photocurrent generation, as the macroscopic performance does, and the charge collection becomes uniform over the full crystallite volume. The results clarify the role of grain boundaries and charge selecting layers and establish the X-ray nanoanalysis techniques as a powerful tool to investigate charge transport and collection in perovskite films.


1. Introduction

X-ray detectors have several applications in many fields, ranging from medical imaging and therapy, basic research, and security. Many applications would greatly benefit from large-area, low-cost, and highly efficient X-ray detectors. Driven by this need, in the last years a lot of effort was put in the study of new functional materials for this purpose. Traditional semiconductors, like amorphous Si and Se, CdZnTe, and others, have many advantages but cannot be easily deposited on large areas due to the complex and energy costly growth methods. One of the alternatives are organic semiconductors that can be deposited from solution at low cost and low temperature^[1]; however, their low atomic number, low charge carrier mobility, and slow time response limit their application.^[2] Metal halide perovskites have emerged as a very promising

alternative to traditional semiconductors and organic semiconductors offering high X-ray absorption and high charge carrier mobility with the possibility to process them from solutions using printing techniques.^[2–4] Efficient X-ray direct detectors based on hybrid perovskite have been reported in the single crystal and thin-film polycrystalline form reaching extremely high sensitivity values up to 10⁵–10⁷ μC Gy⁻¹ cm⁻². As stated in the last review by Kanatzidis's group,^[4] the high performances of the perovskite X-ray detectors reported in literature is related to a poorly understood gain effect. Very recently Gao et al.^[5] demonstrated the possibility of ultrathin perovskite detectors (50 nm) with extremely high sensitivity (10⁵ μC Gy⁻¹ cm⁻²) by combining a CsPbBr₂ layer with an organic semiconductor layer in a transistor architecture. A gain >100 was also reported for perovskite single crystals monolithically integrated onto silicon.^[6] In the latter case, the authors speculated that shallow traps at the perovskite-silicon interface are responsible for activating the gain effect. Glushkova et al.^[7] showed the activation of the gain effect under visible light when a methylammonium-lead-iodide MAPbI₃ (from now on MAPI) pillar is deposited on top of a graphene layer bridging two gold electrodes. The gain was attributed to the defects at the interface between the perovskite and graphene. Another example of the role of interfaces is given by MAPbI₃ combined with [6,6]-phenyl-C61-butyric acid methyl ester fullerene (PCBM), a

M. Verdi, A. Ciavatti, L. Basiricò, F. Boscherini, B. Fraboni
 Department of Physics and Astronomy
 University of Bologna
 Viale C. Berti Pichat 6/2, Bologna 40127, Italy
 E-mail: andrea.ciavatti2@unibo.it; federico.boscherini@unibo.it;
 beatrice.fraboni@unibo.it

J. Segura-Ruiz
 ESRF
 The European Synchrotron
 71 Avenue des Martyrs, Grenoble 38043, France
 R. Sorrentino, I. P. Goncalves, A. Petrozza
 Center for Nano Science and Technology@PoliMi
 Istituto Italiano di Tecnologia
 Via Rubattino 81, Milano 20134, Italy
 I. P. Goncalves
 Physics Department
 Politecnico di Milano
 Piazza L. da Vinci, 32, Milano 20133, Italy

 The ORCID identification number(s) for the author(s) of this article can be found under <https://doi.org/10.1002/aelm.202201346>

© 2023 The Authors. Advanced Electronic Materials published by Wiley-VCH GmbH. This is an open access article under the terms of the Creative Commons Attribution License, which permits use, distribution and reproduction in any medium, provided the original work is properly cited.

DOI: 10.1002/aelm.202201346

well-known organic semiconductor used in perovskite solar cells heterojunctions for its electron affinity and trap passivation ability. Thin films of PCBM and MAPI nanocrystals blends, show a marked increase of the gain effect under visible light thanks to enhanced presence of interfaces.^[8] Recently, simple photoconductor thin films of MAPI nanocrystal covered by a thin layer of PCBM demonstrated high sensitivity under X-rays.^[9] Although no in depth investigations of the role on interfaces have been reported so far, it is clear that they play a crucial role in generating and controlling the gain effect in perovskite visible and X-ray detectors.

X-ray nano-analysis is based on the combination of highly focused X-ray beams and established methods (X-ray diffraction, fluorescence, and X-ray absorption spectroscopy) to investigate materials and devices at the nanoscale. The sample composition and structure can be mapped with nanometer resolution. X-ray nanoanalysis has been previously used to study the role of defects, impurities, and processing in perovskite solar cells at the nanoscale.^[10] Nano X-ray Fluorescence (XRF) mapping has been demonstrated to be effective in revealing the halide migration on MAPbBr₃ single crystals.^[11] The simultaneous acquisition of XRF and X-ray Beam Induced Current (XBIC) has been exploited by Stuckelberger et al.^[12] to study the correlation between charge collection and elemental distribution in perovskite solar cells.

In this paper, we report the use of two-fold X-ray nanoanalysis, performed by simultaneously recording XRF and XBIC signals, to study, for the first time, the effect of a PCBM passivating layer on the performance of perovskite X-ray detectors. We highlight that the use of X-rays as a probe to investigate an X-ray detector produces results related to the device operation mode, thus providing a direct interpretation of the results. The X-ray nanoanalysis experiment was performed at the ID16B beamline^[13] of the European Synchrotron Radiation Facility (ESRF). The performance of this beamline was further boosted with the recently completed EBS upgrade.^[14] The ID16B beamline provides a nano-sized beam and different experimental techniques that can be performed simultaneously. Samples are positioned on a motorized piezo stage capable of fine movements in the plane perpendicular to the incident X-ray beam allowing the scanning of the samples and thus the creation of maps with nanometer resolution. We recorded XRF and XBIC maps on nanocrystalline MAPI detectors for pristine samples and for samples with the addition of PCBM layer (MAPI+PCBM). We developed an original approach to study the correlation between XRF and XBIC signals based on a vectorial representation of color codes in the RGB scheme from which differences between the charge generation and collection in the two detectors can be highlighted. The measured output current is consistently higher at the perovskite grain boundaries of the MAPI samples than in the middle of the grains. In MAPI+PCBM samples, instead, the current signal is uniform over the entire active volume. We extracted the average current density values over several perovskite grains in both types of samples and we defined a parameter to estimate the correlation between the XRF and XBIC signals. The average output current density was found to be higher for the MAPI+PCBM sample with respect to MAPI, confirming that improved performance with the addition of the organic semiconductor is valid also at the nanoscale. The spatial correlation between XRF and XBIC signals was found to be higher for MAPI+PCBM sample

compared to MAPI, with the entire active volume contributing to charge generation and collection uniformly.

Based on the analysis of the X-ray nanoprobe measurements and on previous models of the charge carrier generation in perovskite photodetectors, we propose the following detection mechanism: i) for pristine MAPI a higher gain is present at the grain boundaries due to a higher defect concentration; ii) in MAPI+PCBM the organic semiconductor passivates the traps at the grain boundaries and acts as a sink for electrons which are then transported to the electrodes via the PCBM, while the holes are transported via the perovskite layer. Due to the large difference in the electron and hole mobility, a charge unbalance is generated which, in turn, activates a higher gain in the whole active volume of the detector.

2. Results and Discussion

The synthesis of MAPI perovskite nanocrystals follows a cyclic process based on water and propan-2-ol as solvents, that reduces the precursor dimensions at each step, resulting in MAPI crystals down to hundreds of nanometers. The final solution, composed of perovskite nanocrystals dispersed in propan-2-ol at 100 mg mL⁻¹, is employed for the device fabrication method based on multi-step bar-coating deposition with low toxic solvents, as previously reported in detail.^[8,9] Two types of photoconductor detectors were realized, printed on top of glass substrates with interdigitated gold electrodes with 5 μm channel width. The first type, MAPI, was realized by depositing MAPbI₃ nanocrystal ink on top of the metal contacts. The second type, MAPI+PCBM, was fabricated by adding a second step in the process: after the deposition of the perovskite layer, a PCBM solution was deposited by drop casting on top of the MAPI layer. The PCBM permeates the porous perovskite layer surrounding the perovskite grains. A simple scheme of the MAPI and MAPI+PCBM devices can be found in **Figure 1a**. The MAPI device has the same pattern, without the PCBM layer on top. The perovskite deposition step was repeated to increase the thickness of the active layer up to 5 μm. **Figure 1b** shows the optical microscope image of one sample of MAPI. The thickness of the MAPI clusters is of 5 μm (see line profile in **Figure S1**, Supporting Information) with roughness of 1.24 μm. It has to be noted that we intentionally deposit inhomogeneous film for the purpose of this experiment, to better align the nanobeam into the channel between two electrodes. Continuous films can be obtained if requested by the application. **Figure 1c,d** shows SEM images of the two type of films. The initial MAPI film is porous; thus, it is evident in **Figure 1d** how the polymer permeates through the perovskite nanocrystals. The addition of PCBM layer boosts the performance of the perovskite photodetector in the visible range by enhancing gain factor and response speed.^[8] Recently, we demonstrated the very good performance of the MAPI+PCBM devices in detecting high energy X-ray photons up to 150 keV, that reach X-ray sensitivity of 2270 μC Gy⁻¹ cm⁻², radiation tolerance above 2.2 Gy and fast response time (<50 ms), assessing the possibility to use such solution-based deposition method to create efficient flexible X-ray detectors.^[9] The improved performance due to the addition of the PCBM layer has been associated to its electron acceptor properties, that passivate the traps for majority carriers in the perovskite nanocrystals. These traps are generally associated to grain

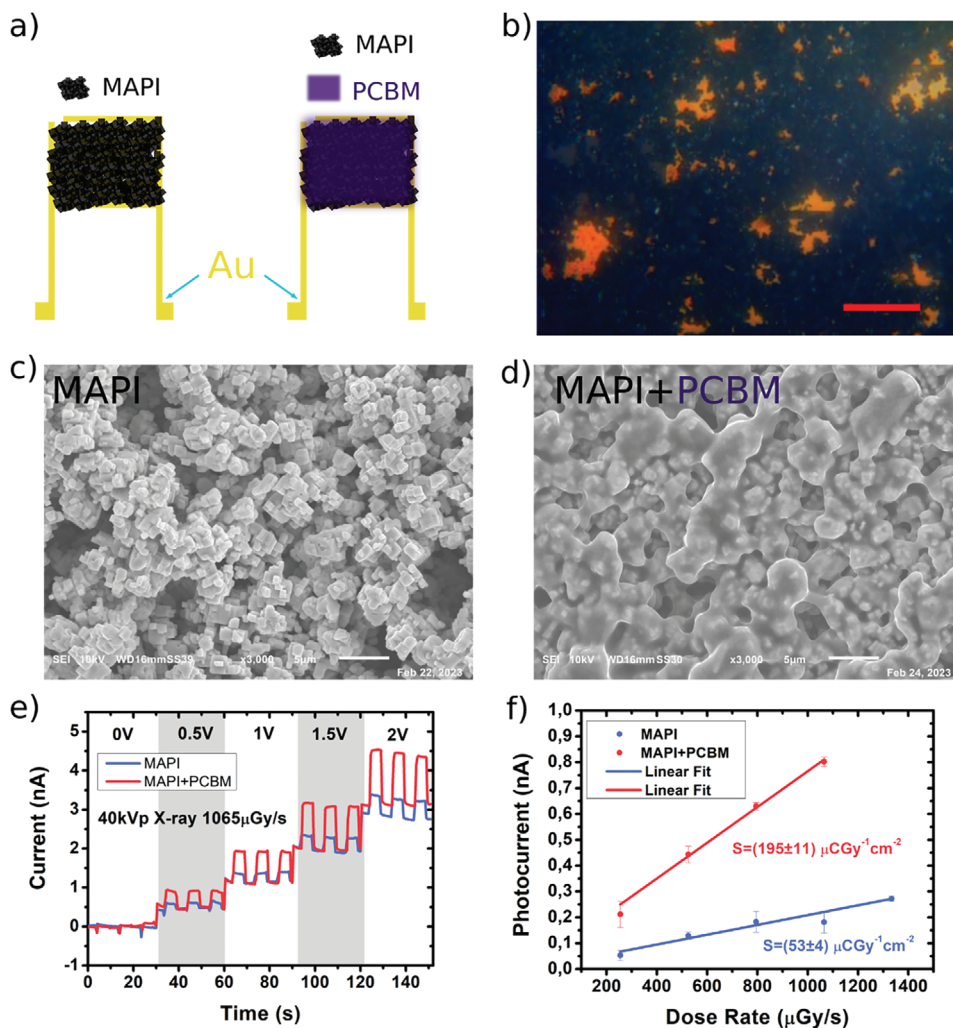


Figure 1. Printed X-ray photoconductor. a) Sketch of the photoconductor detectors fabricated and tested in this work (MAPI and MAPI+PCBM). Both have interdigitated gold metal contacts deposited on a glass substrate. For MAPI (left), the perovskite nanocrystal ink is bar coated on the electrodes. For MAPI+PCBM (right), a PCBM solution is drop casted on top of the MAPI layer as a passivation layer. b) Optical image of MAPI film (read scale bar 50 μm). c,d) SEM images of MAPI c) and MAPI+PCBM d) samples, respectively. Scale bar is 5 μm. e) Dynamic response of MAPI (blue line) and MAPI+PCBM (red line) detectors under 40 kVp X-ray beam with an incident dose rate of 1065 μGy s⁻¹ at different biases (0.5 V, 1.0 V, 1.5 V, 2.0 V). f) X-ray photocurrent as a function of the incident dose rate with 1 V applied bias. The corresponding area normalized sensitivity extracted from the linear fit is indicated with the same color of corresponding data set.

boundaries and are mostly found at the edges of the nanocrystals. However, while it has been hypothesized that trap passivation plays a crucial role in improving the efficiency of perovskites X-ray detectors, this has never been experimentally demonstrated at the microscopic scale. We would like to highlight that the edge regions of the nanocrystalline grains do not, in fact, join to form crystallographically well defined grain boundaries. Rather, they are the edge – near surface regions of the nanocrystalline grains.

With this in mind, we tested the macroscopic X-ray induced current response of MAPI and MAPI+PCBM samples (with an active area of $0.35 \pm 0.01 \text{ mm}^2$) under 40 kVp X-rays. In Figure 1e we report the dynamic response under pulsed X-ray beam for the two types of samples acquired with the same bias between 0 and 2 V and constant dose rate of $1064 \mu\text{Gy s}^{-1}$. Both devices showed box-like response with X-ray induced photocurrent scaling with the bias applied. Noteworthy, the dark current (i.e., the current

flowing in the absence of any radiation) is similar for the two devices for any bias below 2 V while for the highest bias tested (2 V) the MAPI+PCBM samples showed a 10% increase in dark current. However, in the MAPI+PCBM samples, the X-ray induced photocurrent is higher than in MAPI samples at all biases tested. In both types of samples, the X-ray induced photocurrent response is linear with the dose rate and from the slope of the linear fit we extract the sensitivity of the detectors (Figure 1f). The sensitivity at 1 V extracted for the MAPI+PCBM samples is equal to $195 \pm 11 \mu\text{C Gy}^{-1} \text{ cm}^{-2}$ which is almost 4 times higher than the one obtained for pristine MAPI. These results demonstrate that, at the macroscopic device level, the PCBM layer has an active role to increase the detection performance of perovskite X-ray detectors.

To investigate the microscopic role of PCBM at the perovskite-grain interface we performed simultaneous mapping of X-ray

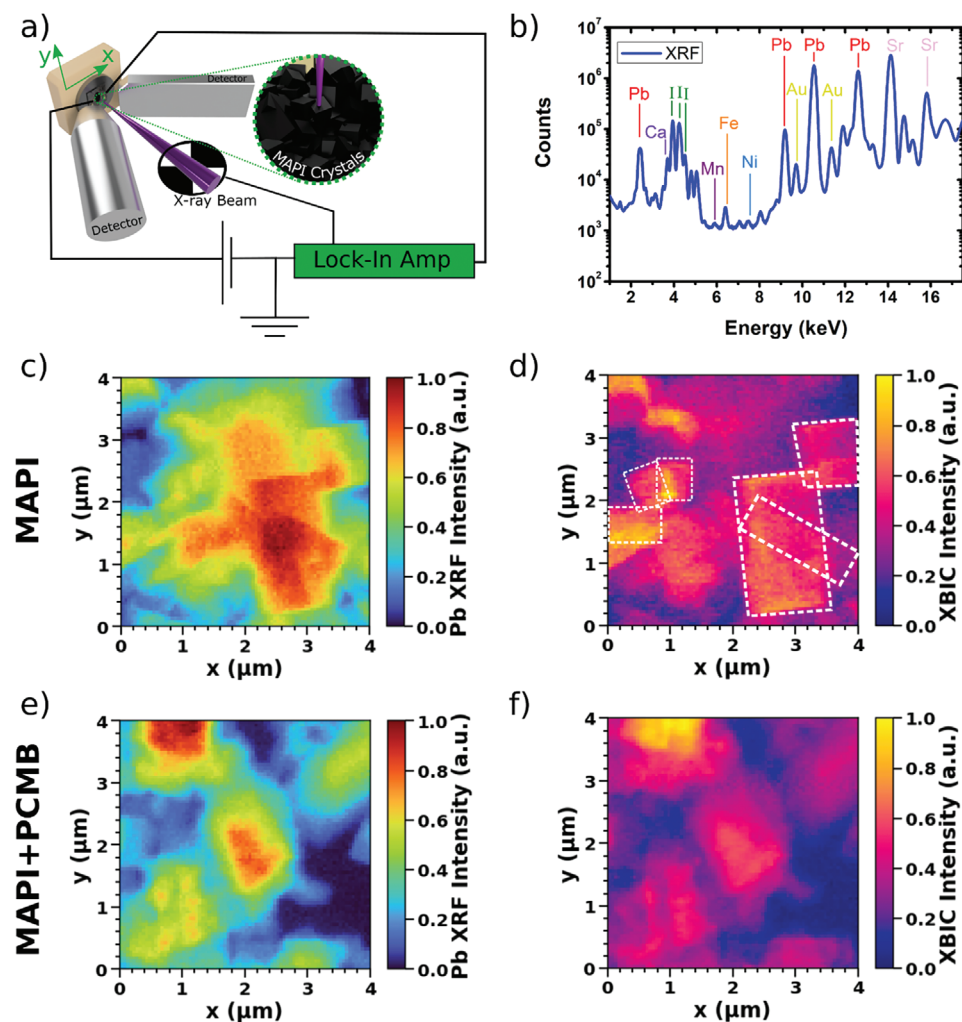


Figure 2. XRF and XBIC mapping. a) Diagram showing the setup used at the ID16B beamline at ESRF. The perovskite sample is mounted on an x-y motorized stage. The X-ray beam is focused down to a 50 nm spot on the sample, smaller than the perovskite grain dimensions. Two detectors are placed near the sample and collect the X-ray fluorescence emitted by it. b) XRF spectrum (average over 11 silicon drift detectors) with the identified peaks from a typical sample measured in this study. Pb and I signals originate in the perovskite while the Au signal comes from the metal contacts. The other emission lines are due to elements present in the substrate. c) Pb XRF map in a 4 $\mu\text{m} \times 4 \mu\text{m}$ area, normalized to (0, 1) for MAPI sample. d) XBIC map at 1 V for MAPI acquired in the same region as the previous Pb XRF map: the boundaries of the perovskite grains are highlighted by dashed white lines. e) XRF and f) XBIC maps for the MAPI+PCMB sample acquired in the same region.

fluorescence (XRF) and X-ray Beam Induced Current (XBIC) at the nanoscale with a 17.5 keV pink beam at ID16B beamline of ESRF Grenoble Synchrotron.^[13] The apparatus is sketched in Figure 2a, showing the sample holder, the silicon drift detectors for XRF signals, and the electric circuit for XBIC measure (see Experimental Section for details). By raster scanning the sample in the plane perpendicular to the beam direction (conventionally labelled x and y), it was possible to construct elemental distribution maps from the fluorescence data. In an X-ray fluorescence spectrum each peak is determined by the emission from the sample of a monoenergetic photon, which is associated to the atomic levels transitions specific to each element. In Figure 2b we report an example of a typical XRF spectrum of the studied MAPI samples with the identification of some relevant observed peaks. The most intense peaks are lead transitions $L\text{I}$, $L\alpha_1$, $L\beta_1$, and $M\alpha_1$ lines and iodine L peaks. The L lines of gold that originate from

the metal electrodes, as well as the K-lines of strontium, calcium, iron, nickel, and manganese are also visible in the spectrum.

Figure S2 (Supporting Information) reports the maps for the elements not directly correlated to the perovskite structure. By comparing these maps with the Pb map of the same region, it is possible to determine whether the signals come from the sample or from the substrate. Fe, Ni, and Mn have a similar distribution to Pb, suggesting their presence in the perovskite grains. On the other hand, the distribution of Sr is the complementary image of the Pb distribution, from which we deduce that the signal comes from the substrate. The distribution of Ca is uniform over the entire region suggesting that it is present in both sample and substrate. Nevertheless, the majority of the XRF signal comes from Pb and I atoms, native of the perovskite molecules, while all the other elements have a small, negligible, contribution. Simultaneously to the XRF spectrum we acquired the XBIC signal, see

experimental section for details. All the maps reported below have been corrected for the geometry of the acquiring detectors and for self-absorption as described in Experimental Section. As our target is the comparison between XRF and XBIC maps in samples with and without PCBM, the extraction of the exact ratio of Pb and I concentrations is beyond the scope of this work.

The X-ray attenuated fraction of 5 μm of MAPI at 17.5 keV is $\approx 13\%$ (Figure S3, Supporting Information), meaning that the majority of the X-ray beam passes through the full film thickness.^[24] However, the X-ray absorption is non-negligible due to the high fluence of the synchrotron radiation. Therefore, as perovskites are known to degrade under intense ionizing radiation, e.g. electrons and focused X-rays beams,^[10] we tested the stability of the devices under the synchrotron beam by acquiring 8 consecutive fluorescence maps of the same region without bias applied between electrodes (reported in Figure S4, Supporting Information). A modification of the Pb distribution is visible just after one scan when acquiring the maps with 500 ms accumulation time and photon flux equal to 10^{12} ph s^{-1} . After 8 scans the shape of the grain is different, as clearly seen in Figure S4a,c,e (Supporting Information). The degradation can be ascribed to photoionization and temperature increase induced by the strong X-ray absorption in the perovskite microcrystals.^[15–17] We were able to significantly reduce the degradation by decreasing the accumulation time (200 ms) and the X-ray flux down to 8.4×10^{10} ph s^{-1} , as shown in Figure S4b,d,f (Supporting Information). No degradation is observed after one scan and only a very slight modification of the Pb distribution is visible after 8 scans. Another crucial attention in dealing with perovskite is the metal interdiffusion from electrodes into the perovskite under radiation and bias.^[18,19] We carefully checked the Au electrodes stability. We observe that high electric field and multiple X-ray exposures promote both perovskite (Pb and I) and electrode (Au) degradation. In Figure S5 (Supporting Information) shows Au XRF maps to follow the electrode degradation over time (4 h 30 min) and bias (1 V, 4 V). At 1 V the Au distribution of the electrode is unchanged at pristine and after 270 min (Figure S5a,b, Supporting Information), while at 4 V the Au electrode completely fall apart in the same amount of time (Figure S5c,d, Supporting Information). To avoid metal interdiffusion issues we acquired the maps only at 1 V. All the data presented in this work were thus acquired under these experimental conditions. Moreover, to further limit the degradation, we did not scan the same region more than two times. All the maps were acquired in a region between the two electrodes, with the direction of the electric field (when applied equal to 1 V) from top to bottom of the reported maps.

The simultaneous acquisition of XRF and XBIC at the nanoscale allows to correlate the elemental distribution and the morphology with the transport and charge collection paths. Figure 2c,d shows the Pb distribution and the XBIC map, respectively, for the same region of a MAPI sample. Variations in the Pb signal are due to the non-uniform thickness of scanned area: regions with no perovskite grains; regions with single crystalline grain and regions with stacked clustered grains. The distributions of I and Au in the same MAPI region of Figure 2c,d are shown in Figure S6a,c (Supporting Information): the distribution in I map is comparable to the one in the Pb map, while the Au signal allows to identify the position of the metal contact. The

perovskite grains are well distinguishable in the XRF map (Figure 2c–e).

If the charge collection efficiency were uniform in the perovskite layer, one would expect the areas with the highest XRF signal to also have the greatest XBIC signal. Since the irradiation area remains constant, regions with higher thickness correspond to higher interaction volume with X-rays and thus a higher number of photo-carriers are generated. In the case of MAPI samples, the XBIC map (Figure 2d) shows a strong photocurrent signal at the grain boundaries and a low signal coming from the bulk region (which instead exhibits higher Pb XRF intensity) of each microcrystal. The missing correlation between XRF and XBIC maps suggests that a photogenerated charge collection is different between the grain surfaces and the rest of crystallite volume. Noteworthy, a different process takes place in MAPI+PCBM samples. Indeed, the XBIC signal is more uniform throughout the crystalline grains (Figure 2f) and it is clearly closely correlated to the XRF Pb map (Figure 2e). This effect becomes more evident when overlapping the XRF and XBIC maps of the same region as shown in Figure 3 for MAPI (a) and MAPI+PCBM (c) samples. The overlaid images are obtained by summing pixel by pixel the red, blue and green values of the XRF and XBIC maps, as better explained in the supporting information (Figure S7, Supporting Information), according to the RGB color model. We normalized the XRF and XBIC maps between 0 and 1 and we assigned the color purple to the Pb XRF signal and green to the XBIC. As a result, purple regions correspond to a dominant XRF signal, green regions to prevailing XBIC signal, and the gray/white areas indicate where the two maps have the same intensity, then correlated.

In the case of MAPI (Figure 3a), a strong contrast between grain boundaries and the grain centers is visible. In the center of the grains, the color purple dominates while the grain boundaries are greener. Instead, the overlaid maps of MAPI+PCBM samples (Figure 3c) appear uniform inside the grains volume and with limited contrast and smooth boundaries. The maps of Figure 3a clearly show the 3D cubic shape of perovskite nanocrystals (some are highlighted in blue dotted lines) with green edges that stand out from the images. The high contrast in the MAPI images confirms the lack of correlation between the XRF and XBIC signals with X-ray current signal that comes mostly from the grain boundaries of the nanoparticles. We extracted line profiles across full grains from the overlaid maps of both MAPI and MAPI+PCBM (Figure 3a–c). The red dotted line on the maps represents the line of profile extraction, while the red rectangle is the area over which the profile is extracted and averaged. The line profiles are reported in Figure 3b–d, below the respective maps. In the MAPI samples, the fluorescence profiles (purple lines) follow the nanocrystal morphology (i.e., central peak with smooth border at the edges); the current profiles (green lines), on the contrary, exhibit pronounced peaks at the borders, corresponding to grain boundaries. In the central graph of Figure 3b, three peaks appear in correspondence to the three edges of the cubic grain. These line profile representations highlight the difference between uncorrelated XRF and XBIC signals. In the case of MAPI+PCBM (Figure 3d), the XRF and XBIC profiles are very similar in shape confirming their high correlation.

For a quantitative comparison between photocurrent generated in samples with and without PCBM, we calculated the X-ray induced sheet photocurrent density values inside the perovskite

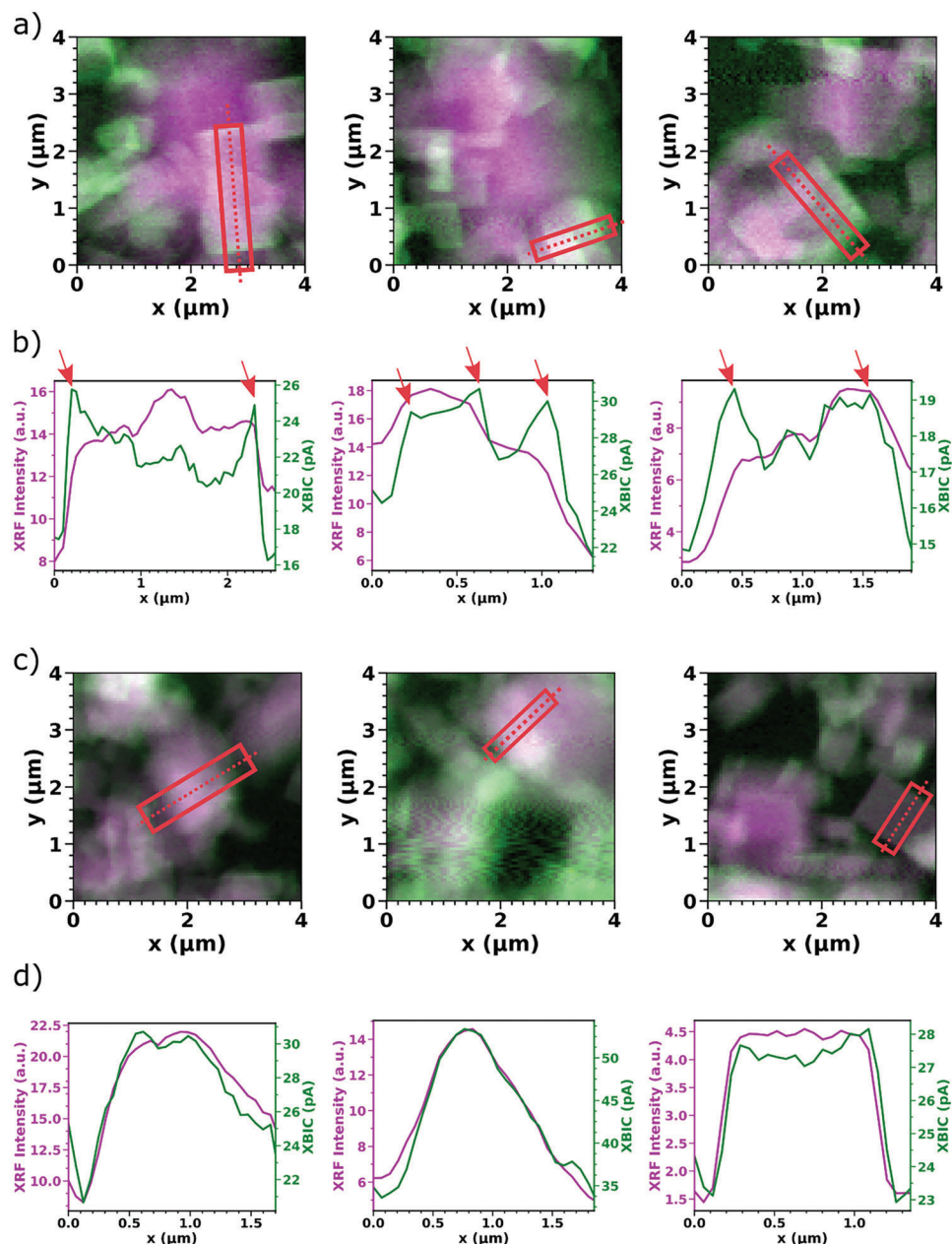


Figure 3. Maps correlation and profile analysis. XRF (in purple) and XBIC (in green) maps overlaid for three different regions in MAPI samples a) and for MAPI+PCBM samples c). The red dashed lines indicate the direction of the line scan, the red rectangles represent the area over which the scan is averaged. The blue dotted lines highlight two grains where the 3D cubic shape is visible. The line profile extractions for MAPI b) and MAPI+PCBM d) are shown below the respective maps: XBIC in green and XRF in purple. The red arrows highlight the position of the grain boundaries.

crystals for the two types of samples. The photocurrent density for each grain was calculated by selecting the region of interest delimitating the crystals' surface area (determined by the Pb XRF maps) with relatively homogeneous perovskite crystals, then integrating the XBIC values over the region of interest and finally normalizing by the area of the region. Though this process, we eliminate the noisy contribution to photocurrent of regions with high inhomogeneity or without perovskite. The analysis was performed over 15 grains in different regions of different samples

and their average results are reported in **Figure 4a**. Despite the high peak values at the grain boundaries of MAPI samples, this analysis confirms that the integrated photocurrent density for each grain of MAPI+PCBM samples is always higher than for MAPI. The average photocurrent density value for MAPI+PCBM samples is $15 \pm 4 \text{ pA nm}^{-2}$, almost twice the value for MAPI, equal to $8.1 \pm 1.4 \text{ pA nm}^{-2}$. It is possible to give a quantitative estimation of the correlation between maps of different physical signals (i.e., XRF and XBIC) by calculating the linear Pearson

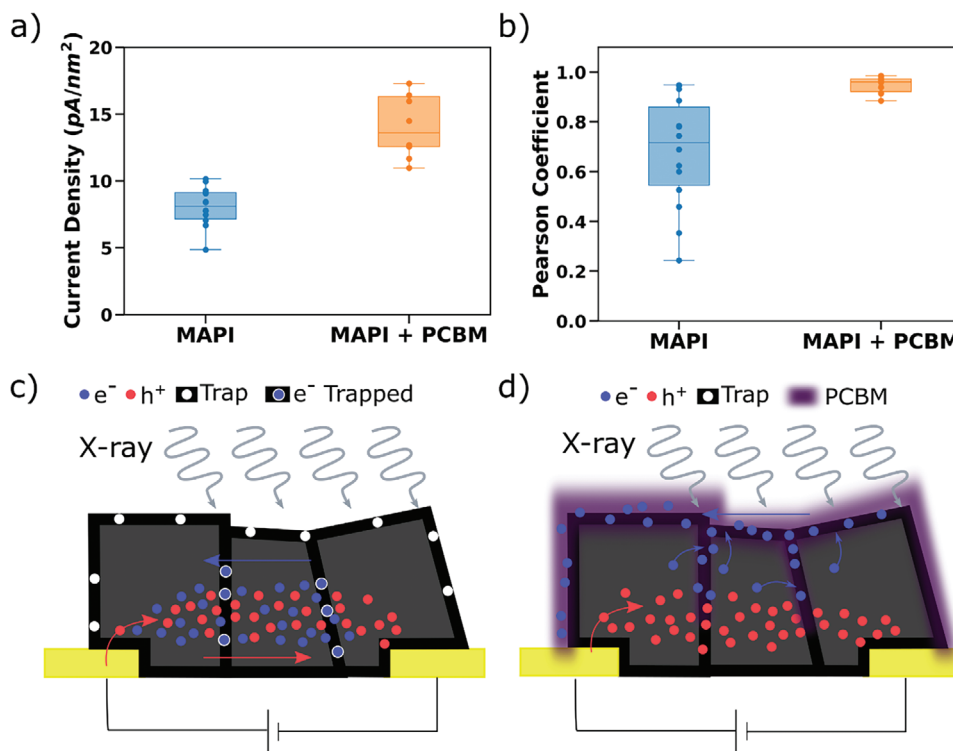


Figure 4. X-ray detection process. a) X-ray Photocurrent density generated inside the perovskite grain, for MAPI (blue) and MAPI+PCBM (orange) obtained by averaging over 15 regions in different samples. b) Linear Pearson Correlation coefficient (Φ) of the XBIC and XRF signals for MAPI and MAPI+PCBM samples. Values averaged over 15 line profiles from different samples. c) Sketch of the charge collection mechanism in MAPI; the electrons (blue dots) are trapped at the grain boundaries and the gain effect takes place as a consequence of charge balancing. d) Sketch of the charge collection mechanism in MAPI+PCBM; the purple shadow region indicates the presence of PCBM at the grain boundaries. The PCBM passivates charge traps and acts as a sink for the electrons. The different mobility in perovskite and PCBM creates a gain effect.

correlation coefficient (Φ) defined as:

$$\Phi = \frac{\sum_{i=0}^N (XRF_i - \overline{XRF}) (XBIC_i - \overline{XBIC})}{\sqrt{\sum_{i=0}^N (XRF_i - \overline{XRF})^2 \sum_{i=0}^N (XBIC_i - \overline{XBIC})^2}} \quad (1)$$

in which XRF_i and $XBIC_i$ are the normalized fluorescence and current signals of the i^{th} point in the line profiles. The XRF and XBIC signals were normalized by mapping the acquired signals between 0 and 1. N is the total number of points in the profile. This quantity increases with the correlation between the line profiles of the XBIC and XRF signals in the same perovskite grain: its value is 1 for perfect overlap, -1 for full anticorrelation, and tends to 0 with decreasing correlation. The linear correlation coefficients for MAPI and MAPI+PCBM maps are reported in Figure 4b. The correlation coefficient of MAPI+PCBM is equal to 0.89 ± 0.03 with a small standard deviation. Instead, the correlation coefficient for MAPI is 0.68 ± 0.12 , a significantly lower with a larger deviation due to scattered values in the plot. The high correlation coefficient in crystallites with PCBM layer, highlights the important role of polymer to improve charge collection in perovskite nanocrystals, allowing an efficient collection of charges from the entire volume of the active layer.

These results, higher current and higher correlation in MAPI+PCBM compared to MAPI, can be ascribed to an elec-

tron sink effect caused by PCBM. Generally, the high responsivity of MAPI perovskite nanocrystalline films with PCBM layer has been ascribed to high photoconductive gain effect, above 200, first for UV-vis photons^[8] and recently has been suggested also for X-rays^[9] in macroscopic photoconductive devices. The X-ray nano-analyses here employed allowed to show the trap passivation effect at the nanoscale and to reveal the role of grain boundaries in the gain process.

Considering a simple MAPI perovskite nanocrystalline films, when the X-ray beam impinges on a region with a high trap concentration (typically grain boundaries) the generated carriers are likely trapped nearby the generation site. If the traps for minority carriers have a detrapping time that is longer than the time needed for the majority carriers to reach the electrode, additional majority carriers are injected from the electrode to maintain the charge balance, as visually illustrated in Figure 4c.

We thus suggest that when PCBM is added on top of the perovskite layer, it permeates through the nanocrystals and passivates the majority carrier traps. In MAPI perovskite the majority carriers are typically associated to holes. PCBM, instead, is an n-type polymer that behaves as an electron acceptor creating a sink for electrons that are generated inside the perovskite grains and are then transported towards the electrode through the PCBM layer (Figure 4d) Assuming the same rate of e-h pairs generation in MAPI and MAPI+PCBM samples under X-rays (the X-ray absorption fraction of PCBM is minor compared to

perovskite), there are two processes that take place in MAPbBr₃/PCBM films: i) the gain is generated by the difference in charge transport paths and mobilities of electrons and holes across the device. Electrons are transferred to the PCBM layer and transported toward the electrodes. The electrons mobility in PCBM is $\approx 10^{-3} \text{ cm}^2 \text{ V}^{-1} \text{ s}^{-1}$,^[20] while the holes mobility in MAPbBr₃ is as high as $100 \text{ cm}^2 \text{ V}^{-1} \text{ s}^{-1}$.^[21] The transit time for holes is then much lower than for electrons and this marked difference in mobility creates a charge unbalance that induces a strong holes injection from metal electrodes in the perovskite layer to regain the charge balance.^[20] In addition, PCBM passivated traps for majority carriers at the interface resulting in more mobile holes that produce a general increase of the gain in photocurrent generation. ii) The electron sink effect of PCBM also subtract X-ray induced electrons for possible recombination improving the holes lifetime. Therefore, holes can be collected from the full crystallite volume, in accordance to a spatially uniform gain effect throughout the grains. The two processes bring to an overall increasing of detectors performance and to the high spatially uniform gain effect. The understanding of these effects at the nanoscale allows the fabrication of more sensitive and more reliable thin film perovskite X-ray detectors.

3. Conclusion

To summarize, we employed X-ray nanoanalysis to study the transport properties at the nanoscale in perovskite MAPbBr₃ nanocrystalline films, by performing simultaneous XRF and XBIC mapping on MAPbBr₃ films with and without PCBM additional layer. We demonstrated the capability of these techniques to reveal at the nanoscale level, high photocurrent generation centers, associated to electron traps, at the grain boundaries of the crystallites in MAPbBr₃ films. On the contrary, in MAPbBr₃/PCBM grains the X-ray photocurrent generation is more than two times higher than in MAPbBr₃, and we showed that the charge extraction is uniform in the full volume of each grain with a correlation coefficient of 0.92 ± 0.02 . These results agree with the experimental observation of macroscopic performance of UV-vis and X-ray devices. They show up at the nanoscale level the importance of PCBM as both, passivating layer and electron sink, as well as the role of grain boundaries in triggering the gain effect in photoconducting devices.

Finally, X-ray nanoanalysis techniques have proven to be powerful tools to investigate perovskite materials and build a bridge between the nano-scale processes with the macroscopic performance of the final devices.

4. Experimental Section

Device Fabrication: The Au electrodes were fabricated by using conventional photolithography, followed by thermal evaporation of Cr (2 nm) and Au (30 nm) on Corning Eagle 2000 glass and Teonex Q65HA–DuPont TeijinFilms. Glass substrates were cleaned by sequential ultrasonication in acetone and isopropanol, 10 min each step. The substrates were treated with oxygen plasma for 10 min before deposition of the perovskite ink. To obtain the ink a cyclic approach was used. A commercial powder of PbI₂ (Sigma Aldrich 99.99%) was slowly added to a MAI (Sigma Aldrich 100 g L⁻¹) solution in isopropanol under stirring at 80 °C. After the addition, perovskite nanocrystals formed and were separated by sedimenta-

tion. Perovskite crystals were then washed with IPA. To restart the cycle water was added; the water molecules break the perovskite structure by dissolving MA⁺ and I⁻ ions in solution. What remained in the solid state were thin sheets of poorly water-soluble PbI₂. The PbI₂ sheets could be used to restart the cycle adding them to MAI solution in IPA. The PbI₂ nanocrystals obtained in this way were smaller in size than the precursor used at the beginning of the process. By using the smaller size precursors, the dimension of the MAPbBr₃ could be reduced. The ink was then deposited by bar-coating (TQC Automatic Film Applicator) in the air. The deposition velocity was set to 30 mm s^{-1} with a bar of 10 μm in diameter. Multiple deposition steps were performed to reach the desired thickness. The passivation layer of PCBM was deposited by drop-casting 30 μL of a 10 mg mL^{-1} solution in chlorobenzene on top of the perovskite layer at 80 °C.

XRF and XBIC Mapping: XRF and XBIC nano-analysis was performed at the hard X-ray beamline ID16B of the ESRF: the European Synchrotron. A pink beam with an energy of 17.5 keV ($\Delta E/E \approx 10^{-2}$) and a photon flux of $8.4 \times 10^{10} \text{ ph s}^{-1}$ was used. Multilayer Kirkpatrick – Baez mirrors focused the X-ray beam down to $60 \times 50 \text{ nm}^2$ (VxH). Two multi-element Si-drift detectors (3 and 7 elements, 50 mm^2 of active area each) detected the XRF signal. Samples were scanned using a piezo-motor stage with a step size of 50 nm, and an accumulation time of 200 ms. The XRF maps were obtained by the sum of the signals of the 10 detectors, the data was fitted using the fit spectra function and using the tool for “matrix correction” implemented in PyMca software in a pixel-by-pixel basis,^[22] to consider the geometry of the detector and the self-absorption of the films that have a significant effect in μm -thick film.^[23] We used the following parameter: incoming angle 90°, outgoing angle 15°, at a distance of 2.5 cm of air, and a mean film thickness of 3 μm . Constant thickness was a strong simplification due to roughness of the film under study. However, the target of this work was the comparison between Pb fluorescence maps in samples with and without PCBM. PCBM was very low interactive with the X-ray, thus the same self-absorption between the two kind of films was considered equal, and a systematic error would be insignificant in this comparison. Fitting results enabled to plot intensity maps for each XRF emission line over the studied area. The XBIC signal was acquired simultaneously by modulating the X-ray beam at 1 kHz and using a lock-in amplifier to improve the signal-to-noise ratio of the signal. The sample was biased at 1 V with an external power supply. The experimental room was kept in air at constant temperature of 23 °C and oxygen of 21%.

Supporting Information

Supporting Information is available from the Wiley Online Library or from the author.

Acknowledgements

The authors acknowledge the European Synchrotron Radiation Facility (ESRF) for provision of synchrotron radiation facilities under proposal number MA-4631 and we would like to thank the beamline staff for assistance and support in using beamline ID16B.

Conflict of Interest

The authors declare no conflict of interest.

Data Availability Statement

The data that support the findings of this study are available from the corresponding author upon reasonable request.

Keywords

perovskite, thin films, X-ray detectors, X-ray nanoanalyses

Received: December 27, 2022

Revised: February 28, 2023

Published online:

- [1] I. Temiño, L. Basiricò, I. Fratelli, A. Tamayo, A. Ciavatti, M. Mas-Torrent, B. Fraboni, *Nat. Commun.* **2020**, *11*, 2136.
- [2] L. Basiricò, A. Ciavatti, B. Fraboni, *Adv. Mater. Technol.* **2021**, *6*, 2000475.
- [3] F. Lédée, A. Ciavatti, M. Verdi, L. Basiricò, B. Fraboni, *Adv. Opt. Mater.* **2022**, *10*, 2101145.
- [4] Y. He, I. Hadar, M. G. Kanatzidis, *Nat. Photonics* **2022**, *16*, 14.
- [5] Y. Gao, Y. Ge, X. Wang, J. Liu, W. Liu, Y. Cao, K. Gu, Z. Guo, Y. Wei, N. Zhou, D. Yu, H. Meng, X. Yu, H. Zheng, W. Huang, J. Li, *Adv. Mater.* **2021**, *33*, 2101717.
- [6] W. Wei, Y. Zhang, Q. Xu, H. Wei, Y. Fang, Q. Wang, Y. Deng, T. Li, A. Gruverman, L. Cao, J. Huang, *Nat. Photonics* **2017**, *11*, 315.
- [7] A. Glushkova, P. Andričević, R. Smajda, B. Náfrádi, M. Kollár, V. Djokić, A. Arakcheeva, L. Forró, R. Pugin, E. Horváth, *ACS Nano* **2021**, *15*, 4077.
- [8] V. Venugopalan, R. Sorrentino, P. Topolovsek, D. Nava, S. Neutzner, G. Ferrari, A. Petrozza, M. Caironi, *Chem* **2019**, *5*, 868.
- [9] A. Ciavatti, R. Sorrentino, L. Basiricò, B. Passarella, M. Caironi, A. Petrozza, B. Fraboni, *Adv. Funct. Mater.* **2021**, *31*, 2009072.
- [10] M. Kodur, R. E. Kumar, Y. Luo, D. N. Cakan, X. Li, M. Stuckelberger, D. P. Fenning, *Adv. Energy Mater.* **2020**, *10*, 1903170.
- [11] Y. Luo, P. Khoram, S. Brittman, Z. Zhu, B. Lai, S. P. Ong, E. C. Garnett, D. P. Fenning, *Adv. Mater.* **2017**, *29*, 1703451.
- [12] M. Stuckelberger, T. Nietzold, G. N. Hall, B. West, J. Werner, B. Niesen, C. Ballif, V. Rose, D. P. Fenning, M. I. Bertoni, *IEEE J. Photovoltaics* **2017**, *7*, 590.
- [13] G. Martínez-Criado, J. Villanova, R. Tucoulou, D. Salomon, J.-P. Suuronen, S. Labouré, C. Guilloud, V. Valls, R. Barrett, E. Gagliardini, Y. Dabin, R. Baker, S. Bohic, C. Cohen, J. Morse, *J. Synchrotron Radiat.* **2016**, *23*, 344.
- [14] P. Raimondi, *Synchrotron Radiat. News* **2016**, *29*, 8.
- [15] E. Lawrence Bright, C. Giacobbe, J. P. Wright, *J. Synchrotron Radiat.* **2021**, *28*, 1377.
- [16] A. Dualeh, P. Gao, S. I. Seok, M. K. Nazeeruddin, M. Grätzel, *Chem. Mater.* **2014**, *26*, 6160.
- [17] M. Rosenthal, D. Doblas, J. J. Hernandez, Y. I. Odarchenko, M. Burghammer, E. Di Cola, D. Spitzer, A. E. Antipov, L. S. Aldoshin, D. A. Ivanov, *J. Synchrotron Radiat.* **2014**, *21*, 223.
- [18] J. Pospisil, A. Guerrero, O. Zmeskal, M. Weiter, J. J. Gallardo, J. Navas, G. Garcia-Belmonte, *Adv. Funct. Mater.* **2019**, *29*, 1900881.
- [19] R. A. Kerner, P. Schulz, J. A. Christians, S. P. Dunfield, B. Dou, L. Zhao, G. Teeter, J. J. Berry, B. P. Rand, *APL Mater.* **2019**, *7*, 041103.
- [20] A. Armin, S. Shoaee, Q. Lin, P. L. Burn, P. Meredith, *Npj Flexible Electron.* **2017**, *1*, 13.
- [21] L. M. Herz, *ACS Energy Lett.* **2017**, *2*, 1539.
- [22] V. A. Solé, E. Papillon, M. Cotte, Ph. Walter, J. Susini, *Spectrochim. Acta, Part B* **2007**, *62*, 63.
- [23] M. Stuckelberger, B. West, T. Nietzold, B. Lai, J. M. Maser, V. Rose, M. I. Bertoni, *J. Mater. Res.* **2017**, *32*, 1825.
- [24] X-Ray Mass Attenuation Coefficients, NIST, **2004**, <https://doi.org/10.18434/T4D01F>.